Stellar cross sections for $^{33}S(n,\alpha)^{30}Si$, $^{36}Cl(n,p)^{36}S$, and $^{36}Cl(n,\alpha)^{33}P$ and the origin of ^{36}S

H. Schatz,* S. Jaag, G. Linker, R. Steininger, and F. Käppeler
Kernforschungszentrum Karlsruhe, IK-III, Postfach 3640, D-76021 Karlsruhe, Federal Republic of Germany

P. E. Koehler† and S. M. Graff
Los Alamos National Laboratory, Los Alamos, New Mexico 87545

M. Wiescher
University of Notre Dame, Notre Dame, Indiana 46556
(Received 26 August 1994)

The cross section of the $^{33}S(n,\alpha)^{30}Si$ reaction was measured in a neutron energy spectrum yielding the stellar rate for a thermal energy of kT=25 keV. For the $^{36}Cl(n,p)^{36}S$ reaction, the experiment was performed in the neutron energy range from 10 to 260 keV. Our new result for ^{33}S resolves the problem of a large discrepancy between two previous experiments. In case of ^{36}Cl it could be shown that the (n,α) channel is negligibly small compared to the (n,p) reaction at s-process conditions. The present results are used for a detailed discussion of a possible s-process origin of the rare neutron-rich isotope ^{36}S.

PACS number(s): 25.40.Ny, 97.10.Cv, 27.30.+t, 29.40.Cs

I. INTRODUCTION

The origin of the elements [1] in the mass range between Si and Fe can be assigned to charged particle reactions during the hydrostatic and explosive burning stages in massive stars [2]. For the synthesis of most of these isotopes, neutron induced reactions are of minor importance. However, there are a few rare neutron-rich isotopes, which are bypassed by charged particle capture reactions. Examples of these species are ^{40}Ar, ^{48}Ca, and ^{36}S.

A first attempt to explain the origin of these isotopes was made by Howard *et al.* [3], who investigated the nuclear reaction network during the high temperatures and densities of explosive carbon burning. In this scenario a pulse was identified with neutron densities intermediate between those typical for the s- and r-processes. This neutron burst is followed by a phase of strong proton irradiation. In this model, a significant production of all rare neutron-rich isotopes was achieved, resulting in substantial overproduction of ^{36}S. However, more recent calculations [4] showed that the effect of explosive nucleosynthesis on the final abundances was overestimated by far in the pioneering work [3].

An alternative site for producing the solar ^{36}S abundance is the s-process during core He burning in massive stars. This scenario corresponds to the weak s-process component [5], which dominates the s-abundances in the mass range between Sr and Se but contributes also to the rare neutron-rich isotopes below iron [2,6–10]. If the production factor of ^{36}S reported by Raiteri *et al.* [10] for a 25 $M_\odot$ star is normalized to those of the s-only nuclei ^{70}Ge and ^{76}Se this scenario accounts for 50% of the solar ^{36}S abundance. This value may be modified by subsequent C burning as well as by the different contributions from a whole generation of stars. The general trend of these results was confirmed by the recent work of Weaver and Woosley [4].

To verify the calculated s-process abundance of ^{36}S, more accurate measurements of the relevant reaction rates are required in the mass range $32<A<40$. The results of two such experiments are presented here: The $^{33}S(n,\alpha)^{30}Si$ cross section has been investigated since the existing data showed differences of a factor 3. In the second experiment, the $^{36}Cl(n,p)^{36}S$ cross section as well as the angular anisotropies and the contribution of the competing (n,α) channel were measured in order to complement the results of a previous study [11].

The improved nuclear physics data were used to study the synthesis of ^{36}S by a network analysis in the relevant mass region between Si and Ca. These calculations were carried out with the nucleosynthesis code NETZ [12] using the parameters from the stellar model of Raiteri *et al.* [10]. The intention of this study was to investigate the effect of the new reaction rates and to establish the main reaction flows from the seed nuclei to ^{36}S for the assessment of the remaining uncertainties.

II. EXPERIMENTAL SETUP

The ^{33}S measurement was performed in a quasi-Maxwell-Boltzmann neutron spectrum [13,14] that al-

*Present address: University of Notre Dame, Notre Dame, IN 46556.

†Present address: Oak Ridge National Laboratory, Oak Ridge, TN 37830.

lowed the determination of the proper stellar cross section for a thermal energy of kT = 25 keV. For the ^{36}Cl measurements, the setup was modified in order to study possible forward/backward asymmetries [15]. In this latter configuration, the neutron spectrum deviates significantly from the ideal Maxwell-Boltzmann spectrum. Therefore, complementary information on the differential cross section for ^{36}Cl [11] was used to determine the stellar cross section.

A. Neutron spectra and flux measurement

The measurements were carried out at the Karlsruhe 3.75 MV Van de Graaff accelerator using the ^{7}Li$(p,n)^{7}$Be reaction for neutron production. During the measurements, the accelerator was operated in DC mode with beam currents of typically 80 μA. Before each run, the accelerator was switched to pulsed operation with a repetition rate of 1 MHz and a pulse width of 10 ns. In this mode, the neutron spectra were measured via the time-of-flight (TOF) technique using a ^{6}Li glass monitor located 83 cm from the neutron target at 0° with respect to the incident proton beam. The targets for neutron production were made of metallic lithium layers, evaporated onto 1 mm thick copper backings.

Two types of lithium targets were used for producing continuous and monoenergetic neutron spectra, respectively. In the former case, relatively thick targets (10 μm) were used, and the proton energy was adjusted to E_p=1912 keV. Under these conditions, the resulting neutrons are emitted in a forward cone of 120° opening angle and the angle-integrated neutron spectrum resembles a Maxwell-Boltzmann distribution for kT=25 keV [13,14]. This spectrum was used in all ^{33}S runs, directly yielding the stellar cross section for a thermal energy of kT=25 keV. With the different setup in the ^{36}Cl experiment (Sec. II B), the sample was too small to cover the entire neutron cone. In this case, the effective neutron spectrum at the sample position was calculated by a Monte Carlo code using the angular distribution values of Ratynski and Käppeler [14]. Although the spectrum differed somewhat from the stellar situation it was broad enough to average over single resonances. The corresponding 14% correction for the proper stellar cross section was determined using the differential cross section of Koehler *et al.* [11].

For ^{36}Cl, additional thin (2.5 μm) lithium targets were used to yield monoenergetic spectra at higher energies. Before and after these runs, the neutron spectra were characterized via TOF measurements by switching the accelerator to pulsed mode. In this way it was verified that the neutron spectra were not deteriorated by target buildup. In total, four different neutron spectra with a typical FWHM of 30 keV were used to cover the energy range from 100 to 260 keV. The proper neutron spectra seen by the sample were calculated from the measured 0° spectra after unfolding the time resolution. To account for the proton energy losses in the Li layers, the 0° neutron spectra were subdivided in typically ten energy bins. The respective neutron spectra emitted into the solid angle of the sample were calculated with a Monte Carlo code, using the angular distributions of Liskien and Paulsen [16]. The effective spectrum was then obtained by summation over all bins after weighting with the ^{7}Li(p,n) cross section.

The time-integrated neutron flux was measured by activation of a 30 μm thick gold foil mounted back-to-back with the sample [17] as indicated in Fig. 1. The evaluated flux is based on the differential gold neutron capture cross section of Macklin [18] normalized to the 25 keV value of Ratynski and Käppeler [14]. The corrections for slightly different neutron fluxes due to the small distance between gold foils and sample were measured using

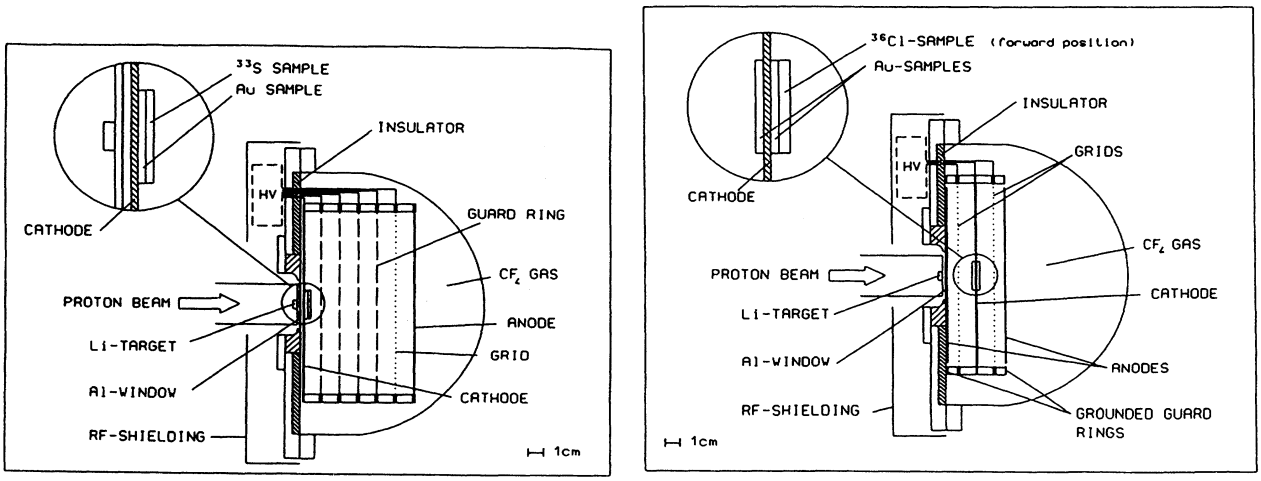

FIG. 1. Experimental setup for the measurement of (n,α) and (n,p) cross sections, showing the arrangement of neutron production target and ionization chamber for the detection of α particles and protons, respectively. Left: Samples close to neutron target for direct determination of stellar cross section (^{33}S). Right: Neutron target and samples separated by 19 mm for measurement of forward/backward asymmetries (^{36}Cl).

a second gold foil instead of the sample. Corrections for neutron attenuation by either one of the samples or the cathode (always <0.4%) as well as for variations of the neutron yield with time (always <0.05%) were negligibly small. The overall uncertainty in the flux determination was typically 2–3 % (Sec. III A).

B. Ionization chamber

The emitted charged particles were detected using a parallel-plate ionization chamber, which has the advantage of a 100% efficiency (verified to ±1% with a calibrated ^{241}Am source) within a solid angle of practically 2π (Sec. III D). An axial chamber geometry was chosen for the present setup to obtain a homogeneous field distribution even for a large entrance window.

1. Setup for the ^{33}S measurement

The mechanical construction as sketched in the left part of Fig. 1 was originally planned for application with the quasi-Maxwell-Boltzmann spectrum described above, where all neutrons are emitted in a forward cone with a 120° opening angle [19,17]. Therefore, the base plate carrying the entire structure with cathode, guard rings, Frisch grid, and anode was built with a thin window at the center in order to minimize the source-to-sample distance. The hemispherical lid of 0.5 mm thick stainless steel was sufficiently separated from the sample that neutron scattering corrections become negligible. In this version, the diameter of the active volume was 142 mm at a cathode-anode spacing of 65 mm. The Frisch grid consisted of 0.03 mm thick tungsten wires with a 0.75 mm spacing. The insulating structure was made of ceramic material, and the voltage divider for the connection of guard rings and anode was mounted on the outside of the chamber for easier access.

During the experiments, a continuous gas flow was maintained for stable operation. The gas pressure was kept within ±1 mbar of the selected value by means of a regulation circuit including a sufficient buffer volume. CF_4 was found to be the best choice for the counter gas, because compounds containing hydrogen had to be omitted in order to avoid background from recoil protons. The energy resolution of about 100 keV was measured using a mixed ^{239}Pu/^{241}Am/^{244}Cm α source. This same source together with the ^{6}Li$(n,\alpha)^3$H and the ^{10}B$(n,\alpha)^7$Li reactions served for verification of a linear energy response.

2. Setup for the ^{36}Cl measurement

The above setup was modified to obtain a twin chamber to allow forward and backward measurements thus covering a solid angle of almost 4π [20]. This was achieved by adding another Frisch grid and anode and by reducing the cathode-anode distance to 18 mm (right part of Fig. 1). The diameter of the active volume was reduced to 90 mm. With this geometry, the resolution for the α lines from the ^{239}Pu/^{241}Am/^{244}Cm source could be improved to 60 keV. On the other hand, the effective neutron flux at the sample position was reduced by about a factor 10, and the determination of the true neutron spectrum became more difficult (Sec. II A).

C. Samples

^{33}S. The main difficulty in preparing the sulfur samples was due to the volatility of this element. Therefore, two complementary methods have been used, ion implantation and deposition from a solution.

Sufficiently homogeneous sulfur layers of 20 mm diameter could be produced by ion implantation. To study the stability of these layers, Rutherford backscattering (RBS) analyses were performed before and after aging the samples. It was found that heating the samples to 55 °C for 100 min and storing them under the conditions of the experiment (15 h in CF_4 at a pressure of 300 mbar) reduced the sulfur content of the implanted layer by 15%. Therefore, the samples had to be checked for possible losses after the experiment.

The actual samples were implanted into disks of spectroscopy grade carbon, 30 mm in diameter and 0.7 mm thick, starting from isotopically enriched material (14.9% ^{33}S). The implantation was carried out with an energy of 300 keV and an average beam current of 0.4 μA. It lasted for 6.4 h, corresponding to a total number of 5.5×10^{16} implanted atoms. The contamination with ^{32}S atoms was determined from the mass resolution of the ion implanter (measured with natural sulfur) resulting in a ^{33}S enrichment of 96±4%.

The total amount of sulfur in the sample was determined via RBS using an α particle beam of 2 MeV and a detection angle of 165°. The quality of the implanted layers is illustrated in Fig. 2, which shows an RBS spectrum before and after the experiment. One finds that almost all of the implanted sulfur is concentrated in a 73 μg/cm^2 thick layer covered by 46 μg/cm^2 of carbon. Obviously,

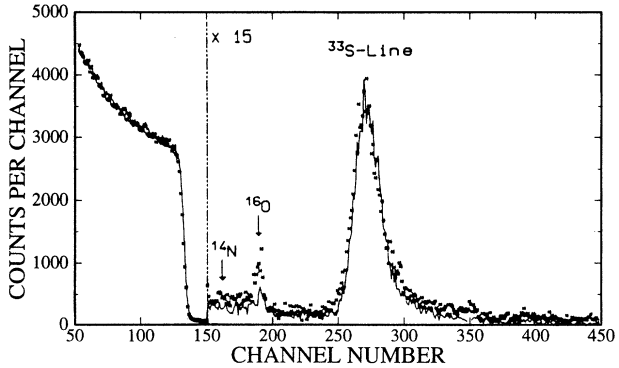

FIG. 2. Rutherford backscattering spectrum of the implanted ^{33}S sample before (solid line) and after the experiment (stars). The implanted layer remains remarkably stable; the only noticeable difference between the spectra refers to an increase of nitrogen and oxygen at the surface.

the sulfur distribution remained unchanged during the experiment, which means that the losses observed in the aging test must have been due to the additional heating. The nitrogen and oxygen that were deposited at the surface did not affect the actual measurement. Normalization of the yields obtained for sulfur and for the carbon matrix with the respective RBS cross sections results in a sample thickness of $(1.64\pm0.08)\times10^{16}$ cm^{-2}. The total amount of ^{33}S in the sample, $N_{33}=(5.17\pm0.41)\times10^{16}$, was eventually determined from the thickness, the ^{33}S concentration, and a careful measurement of the implanted area. This number is in fair agreement with the 5.30×10^{16} atoms deduced from the accumulated charge during the implantation.

The second method for preparing suitable sulfur samples was deposition from a well-defined solution. The problem with this technique is that the samples exhibited significant inhomogeneities, which require larger self-absorption corrections. To minimize this effect, small droplets of about 5 μl K_2SO_4 solution were put onto an alumium oxide layer in a regular pattern with the aim of obtaining samples of 28 mm diameter and a total of $\sim5\times10^{17}$ ^{33}S atoms. The porous structure of freshly prepared aluminium oxide absorbs the solution more uniformly than a smooth surface. Layers of 6 and 24 μm (S/Al3 and S/Al2, S/Al4, respectively, see Table I) were prepared by electrolytic oxidation, and K_2SO_4 solutions with different concentrations were applied in a very humid atmosphere in order to delay the drying process until the droplets had sufficiently spread out. On the thin aluminum oxide layers, small crystal structures with a typical size of 4 μm could still be observed, which quickly dried in normal air to a whitish appearance. The thicker oxide layers seemed to absorb the solution much better, since no crystals could be observed even under a microscope. In order to study the homogenizing effect of the aluminum oxide layers, a sample on a gold foil was prepared in the same way, except that the droplets remained separated in this case. The final uncertainty in the number of ^{33}S atoms is between 2 and 3%, considerably smaller than for the implanted sample. (For a detailed discussion see Ref. [19].)

All samples used in this work are summarized in Table I. It is worth noting that the traditional mass determination by weighing was not adequate for the very small masses of all sulfur samples.

^{36}Cl. Only one sample was available for this radioactive isotope. It was prepared by vacuum evaporation of sodium chloride onto a 25 μm thick aluminum foil as described by Koehler *et al.* [11]. The chlorine was enriched to about 55% in ^{36}Cl, and the total number of ^{36}Cl atoms on the sample was measured to be $N_{36}=(2.68\pm0.11)\times10^{18}$ by comparison with a reference source from the U.S. National Bureau of Standards. The sample had a nominal diameter of 20 mm, but showed a diffuse edge on one side. The influence of this defect on the cross section was investigated by Monte Carlo calculations for all neutron spectra and for different assumptions on the ^{36}Cl distribution and was always about 1%. Therefore, this correction was neglected, but a systematic uncertainty of 2% was considered instead. In spite of the sample activity of 2 MBq, the decay electrons had no effect on the performance of the ionization chamber.

^{197}Au. For the determination of the neutron flux, in each run a 30 μm thick gold foil was placed in the ionization chamber, back-to-back with the investigated sample (Fig. 1). The diameter of the gold foil was always equal to that of the sample.

TABLE I. Sample characteristics.

Isotope	Sample	Chemical form	Diameter (mm)	Mass (μg)
^{33}S	S/Cl	implanted	20	2.83±0.22
^{33}S	S/Al2	K_2SO_4	28	27.45±0.58
^{33}S	S/Al3	K_2SO_4	28	27.56±0.55
^{33}S	S/Al4	K_2SO_4	28	50.74±1.47
^{33}S	S/Au5	K_2SO_4	28	43.39±1.00
^{36}Cl	Cl/Al1	NaCl	20	160.2±6.4

III. MEASUREMENTS AND DATA ANALYSIS

A. Neutron flux

In all experimental runs, the neutron flux was measured by means of an activated gold foil as described above. The uncertainty in the flux determination was dominated by the gold neutron capture cross section (±1.5%) and the efficiency calibration of the Ge detector (±1.5%), whereas counting statistics (< ±1.0%) and self-absorption corrections (±0.2%) were less important. The correction for the flux difference due to the back-to-back geometry was ~3%, except for the implanted ^{33}S sample, where the thicker backing required a 7% correction. The respective uncertainties were 0.8% and 1.8%. Minor contributions to the systematic uncertainty resulted from the corrections for neutron attenuation (±0.2%), for the relative γ-ray intensity per decay in ^{198}Au (±0.1%), as well as for the neutron flux variations during the measurements (±0.05%). Another small uncertainty was due to the correction of the Ge-detector efficiency for the fact that the actual samples were larger than the pointlike γ-ray sources used for calibration (±0.2%). In summary, the uncertainty in the determination of the neutron flux was typically 2.4%, except for the measurements with the implanted ^{33}S sample, where the total uncertainty was 2.9%.

B. The ^{33}S measurements

Measured pulse height spectra for the ^{33}S(n,α) reaction (E_α=3.1 MeV) are displayed in Fig. 3. The spectra obtained with the implanted and with two of the deposited samples differ significantly. The advantage of the implanted sample with respect to the correction for self-absorption is obvious, whereas the line shapes of the deposited samples exhibit a significant tailing towards

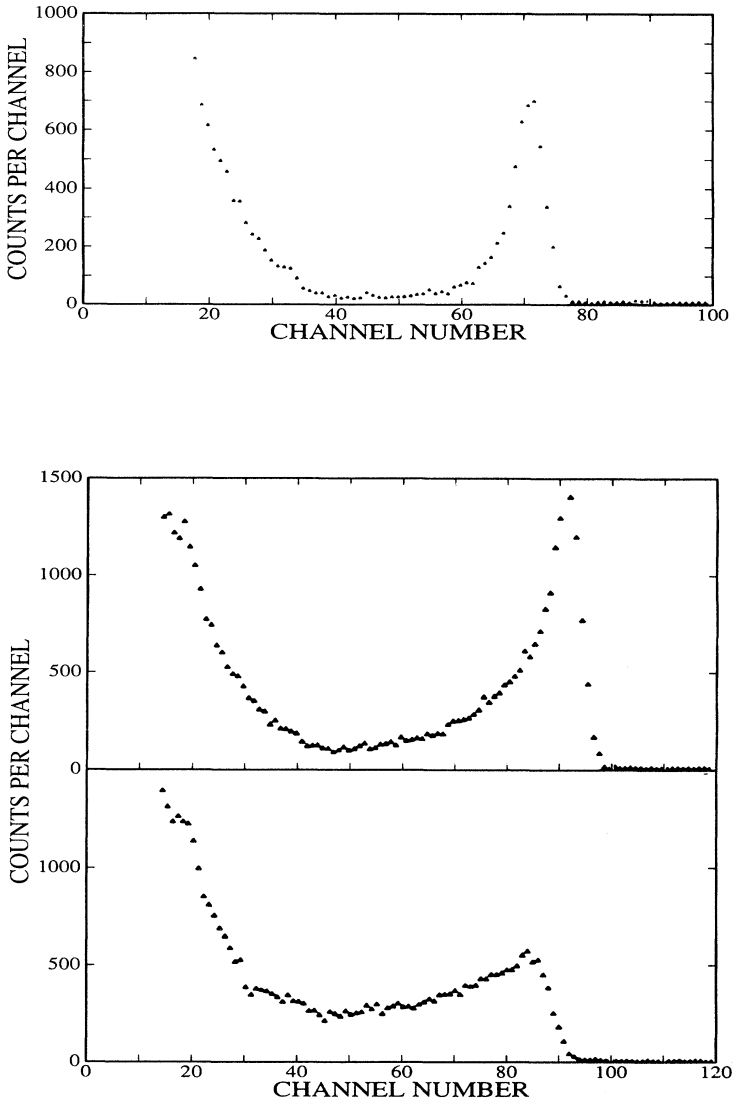

FIG. 3. Pulse height spectra from the $^{33}S(n,\alpha)$ measurement. Top: Spectrum taken with the implanted sample (Run S/C1). Middle: spectrum of one of the thin samples deposited on aluminum oxide (Run S/Al2). Bottom: spectrum obtained with the sample deposited on gold foil (Run S/Au5). The sample quality decreases from top to bottom due to increasing inhomogeneities.

lower energies due to sample inhomogeneities. This effect is largest for the sample deposited on the gold foil. In this spectrum, the α peak appears also shifted by 0.24 MeV.

C. The ^{36}Cl measurements

Protons from the $^{36}Cl(n,p)^{36}S$ reaction are emitted at an energy of 1.9 MeV plus the incident neutron energy, and only the ground state of ^{36}S can be populated at the neutron energies used herein. In the case of the $^{36}Cl(n,\alpha)^{33}P$ reaction only the 2.2 MeV α line from the ground state transition was observed. Transitions to excited states are possible but are expected to be very weak due to the much lower α energies ($E_\alpha < 1$ MeV) available for Coulomb barrier penetration.

The protons and α particles had to be separated by performing two independent measurements. First, the gas pressure in the ionization chamber was set to 2000 mbar, which was sufficient to stop the protons and α particles within the active volume of the detector. The corresponding pulse height distributions measured in the broad neutron spectrum with an average energy of 52 keV are shown in Fig. 4. In the upper panel, the 1.9 MeV proton line appears well separated from the background and with good resolution, confirming the quality of the sample.

In the runs with the high gas pressure the 2.2 MeV α line could not be resolved from the 1.9 MeV proton line. Therefore, the α particle contribution had to be measured in separate runs with a reduced gas pressure of 600 mbar. This was chosen to stop the 2.2 MeV α particles inside the active detector volume. Under these conditions, the 1.9 MeV protons could only deposit a small fraction of their energy and appeared at lower pulse heights, well separated from the α particles. A corresponding pulse height distribution is given in the lower part of Fig. 4, showing the 2.2 MeV α line as well as the upper edge of the proton distribution, which is broadened due to the

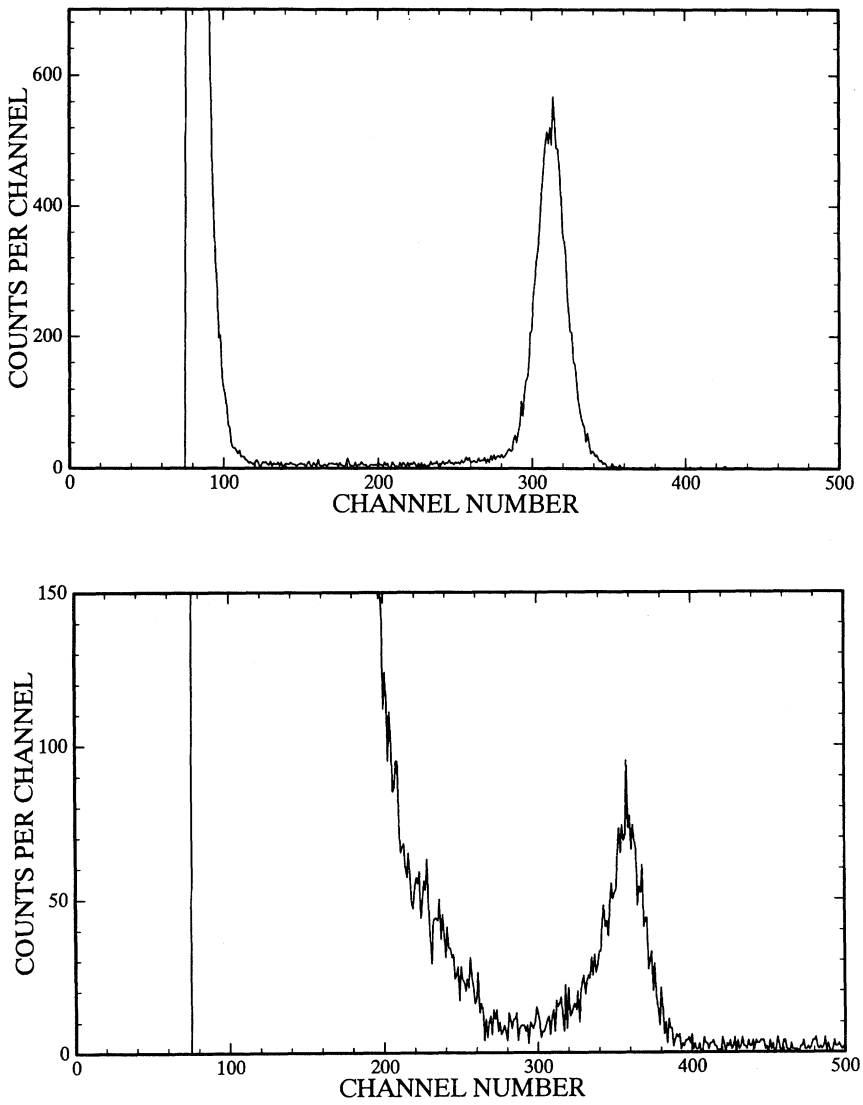

FIG. 4. Pulse height spectra from the ^{36}Cl measurement obtained for the broad neutron spectrum with 52 keV average energy. Top: The proton spectrum taken at a gas pressure of 2000 mbar. Bottom: The spectrum after the gas pressure was reduced to 600 mbar, showing the α line and the edge of the broad proton distribution.

angle-dependent path lengths in the active detector volume.

For each proton or α measurement two independent runs were performed with the sample in the forward and in the backward direction. In this way, a solid angle of almost 4π could be covered (Sec. III D), and the measured forward/backward ratio provided additional information on the reaction.

D. Spectrum analysis

For each run, the background was corrected by subtraction of spectra taken with blank sample backings. The background in the critical energy region was mainly produced via the ^{10}B$(n,\alpha)^{7}$Li reaction on boron contaminations in the detector and target materials and was very small as can be seen in Figs. 3 and 4.

An important aspect in analyzing the experimental spectra was the determination of the effective solid angle of the detector, including corrections for self-absorption effects due to particles emitted at angles close to 90° with respect to the beam axis. Because the background subtracted spectra exhibit large statistical uncertainties at lower pulse heights, events below a certain energy threshold of typically 1 MeV could not be detected. This energy threshold corresponds to a maximum emission angle thus resulting in a slight reduction of the effective solid angle. This correction is particularly important for the ^{33}S samples on aluminum or gold backing (Fig. 3).

The fraction of events falling below the energy threshold was determined analytically [21] as well as with a Monte Carlo simulation of the measured α and p spectra. For both methods isotropic emission of the reaction products was assumed, although this may not be strictly valid. Therefore, a generous uncertainty of 50–100 % was adopted for this correction. It turned out that the analytic solution [21] could only be applied to the spectra obtained from the sufficiently uniform samples, for exam-

ple from the implanted ^{33}S and the evaporated ^{36}Cl layers. For these, the efficiency corrections were 5±2% and 2±2%, respectively. The inhomogeneities of the K_2SO_4 deposits required a two-component Monte Carlo fit for an adequate description of the pronounced tailing in the line shapes. Therefore, the resulting corrections and uncertainties were much larger, ranging from 9±5% for the thinner aluminum oxide sample up to 35±33% for the deposit on gold.

Additional smaller corrections of the evaluated particle yields had to be applied to account for anisotropic emission due to the center-of-mass velocity (0.5–1 %) and to the backscattering of α particles from the sample and/or from the backing. These backscattering corrections were 0.5%, 0.8%, and 3.9% for carbon, aluminum, and gold backings, respectively.

IV. EXPERIMENTAL RESULTS

A. ^{33}S measurement

With the data and corrections discussed so far, the cross sections for the $^{33}S(n,\alpha)^{30}Si$ reaction can be expressed as

$$\sigma = 2\frac{C}{N \times \Phi}, \tag{1}$$

where C is the α particle yield including all corrections discussed above, Φ is the time-integrated neutron flux, N the number of target nuclei per sample area, and the factor of 2 accounts for the solid angle of 2π.

The results for ^{33}S are listed in Table II together with the statistical and systematic uncertainties. In all runs, the correction for undetected events due to energy losses of reaction products in the sample dominates the overall uncertainty. If plotted versus this correction (Fig. 5), the results seem to be systematically lower for the runs with larger absorption, a possible indication that the Monte Carlo fits were not completely adequate. However, the respective uncertainties are so large for the runs with large corrections that these values have almost no impact on the final result.

The resulting mean value of 183±9 mb required one more correction to account for small deviations of the experimental neutron spectrum from the ideal spectrum yielding the true stellar cross section. This correction factor was determined to be 0.96±0.01 by comparison of the average cross section for the experimental spectrum

TABLE II. Measured ^{33}S cross sections at kT=25 keV.

Run	Sample	σ (mb)	$\Delta\sigma_{stat}$ (mb)	$\Delta\sigma_{syst}$ (mb)
S1	S/C1	184.8	±3.2	±17.1
S2	S/C1	176.4	±3.0	±16.0
S3	S/Al2	163.3	±1.5	±30.7
S4	S/Al3	197.8	±2.4	±12.4
S5	S/Al4	155.5	±2.0	±21.4
S6	S/Au5	168.6	±1.9	±57.3

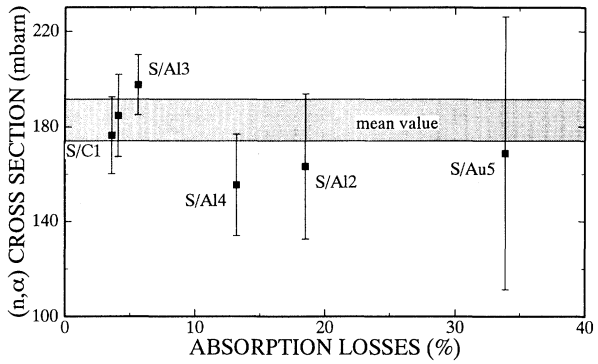

FIG. 5. The $^{33}S(n,\alpha)$ cross sections measured with different samples versus the respective absorption losses. The weighted mean is dominated by the runs with the thinnest samples.

and for the ideal case using the differential data of Wagemans *et al.* [22]. Finally, the stellar cross section of the $^{33}S(n,\alpha)^{30}Si$ reaction at kT=25 keV was found to be

$$\frac{\langle\sigma \times v\rangle}{v_T} = 175 \pm 9 \text{ mb}. \tag{2}$$

Extrapolation of this result to the standard s-process temperature of 30 keV as well as to the higher temperatures during carbon burning or in explosive scenarios can also be obtained via the differential data [22]. These values are listed in Table V for comparison.

The present result solves the problem of the large difference between the measurements of Auchampaugh *et al.* [23] and of Wagemans *et al.* [22], where stellar cross sections of 690±170 and 227±20 mb at 30 keV were reported, respectively. There is also agreement with the cross section of 224 mb calculated via the statistical model [24].

B. ^{36}Cl measurement

In this case, the different geometry requires a modification of Eq. (1) for describing the cross section

$$\sigma = \frac{C_b}{N \times \Phi_b} + \frac{C_f}{N \times \Phi_f \times (1-K)^2} = \frac{C_b}{N \times \Phi_b}\frac{1+f}{1-K}. \tag{3}$$

Here, C_f and C_b are the forward and backward particle yields including the corrections for absorption losses of the reaction products within the sample. Φ_f and Φ_b are the time integrated neutron fluxes for the measurements in forward and backward direction, N the number of target nuclei per sample area, and K the correction for the center-of-mass velocity. The forward/backward ratio of the emitted particles f can be obtained by

$$f = \frac{\Phi_b C_f}{\Phi_f C_b (1-K)} - K. \tag{4}$$

It is defined as the forward/backward ratio of the particles emitted by the target nuclei in the center-of-mass

TABLE III. Measured ^{36}Cl(n,α) cross sections and anisotropies.

	Neutron spectra		Results					
Run	av. E_n (keV)	FWHM (keV)	σ (mb)	$\Delta\sigma_{stat}$ (mb)	$\Delta\sigma_{syst}$ (mb)	f	Δf_{stat}	Δf_{syst}
Cl6	52	[a]	0.90	±0.037	±0.092	1.1	±0.063	±0.19
Cl7	181	28	<0.2	...	...	...	...	...
Cl8	222	28	0.89	±0.068	±0.077	...	...	...

[a]Broad neutron spectrum resembling a Maxwell-Boltzmann shape; see Sec. II A.

system. Because of the fact that f is measured in respect to the symmetry axis of the detector, which is, due to the divergence of the neutron beam, not identical to the direction of the incident neutrons, an additional uncertainty of about 5% had to be added to obtain the anisotropy of the involved nuclear reaction.

The results from the ^{36}Cl$(n,\alpha)^{33}$P experiment, which was the first measurement of this cross section in the energy range of astrophysical interest, are presented in Table III. The cross section obtained at 52 keV exhibits a systematic uncertainty of 10%, which is mostly due to the correction for self-absorption effects, the uncertainty of the sample mass, and the neutron flux determination. The uncertainty of the corresponding forward/backward ratio is almost completely determined by the correction for self-absorption. Within uncertainties, the forward/backward ratio in the (n,α) reaction is consistent with isotropy. The count rate at 181 keV was so low, that only an upper limit for the cross section can be given. The measurement at 222 keV neutron energy was performed in forward direction only, and the forward/backward ratio at 52 keV (1±0.2) was adopted for obtaining the cross section value.

The measured ^{36}Cl$(n,p)^{36}$S cross sections are listed in Table IV. The systematic uncertainties of $\sim$ 6% arise mainly from the uncertainties in sample mass and neutron flux. The comparison with the (n,α) results shows that the 1% contribution from the ^{36}Cl$(n,\alpha)^{33}$P channel can be neglected in view of the other uncertainties. The measured forward/backward ratios of the (n,p) channel show small but significant deviations from isotropy, indicating the influence of p-wave resonances as assumed by Koehler *et al.* [11].

The (n,p) cross sections can be compared to the previous data of Koehler *et al.* [11] by folding their differential values with the present neutron spectra. This folding procedure was found to be insensitive to the uncertainties in the respective neutron spectra, despite the resonance structure in the differential data [11]. As can be seen from Fig. 6, excellent agreement was obtained in the entire energy range up to 200 keV. The new results at 222 and 244 keV are 20 and 30 % lower than the values of Koehler *et al.* [11], but still consistent within uncertainties.

Apart from the verification of the (n,p) cross section, the present results complement the experiment of Koehler *et al.* [11] in two relevant points: (i) It was shown that the (n,α) channel is indeed negligible compared to the (n,p) cross section as assumed in their analysis. (ii) From the relatively small deviations of the measured forward/backward ratio from isotropy as well as from the good agreement between the two experiments it can be concluded that angular distribution effects had no significant impact on the results of Koehler *et al.* [11], although their detector covered only a limited solid angle around 90° with respect to the neutron beam.

From the present data a stellar cross section for the ^{36}Cl$(n,p)^{36}$S reaction at kT=30 keV of

$$\frac{\langle\sigma \times v\rangle}{v_T} = 91 \pm 8 \text{ mb} \quad (5)$$

was derived, in excellent agreement with the result of Koehler *et al.* [11]. This value is over two times smaller than the previously recommended value of 205 mb [25], which was based on the statistical model calculations [24]. The stellar cross sections for a range of thermal energies are listed in Table V. These values were calculated by normalizing the data of Koehler *et al.* [11] to the present results. While there is perfect agreement at kT=30 keV, the new 100 keV value is about 10% lower than reported in Ref. [11].

TABLE IV. Measured ^{36}Cl(n,p) cross sections and anisotropies.

	Neutron spectra		Results					
Run	av. E_n (keV)	FWHM (keV)	σ (mb)	$\Delta\sigma_{stat}$ (mb)	$\Delta\sigma_{syst}$ (mb)	f	Δf_{stat}	Δf_{syst}
Cl1	52	[a]	93	±2.9	±5.5	1.08	±0.018	±0.040
Cl2	152	26	35	±1.1	±2.0	1.21	±0.020	±0.031
Cl3	181	28	26	±0.81	±1.5	1.08	±0.017	±0.031
Cl4	222	28	24	±0.77	±1.5	1.32	±0.051	±0.085
Cl5	244	29	24	±0.55	±1.6	0.77	±0.015	±0.060

[a]Broad neutron spectrum resembling a Maxwell-Boltzmann shape; see Sec. II A.

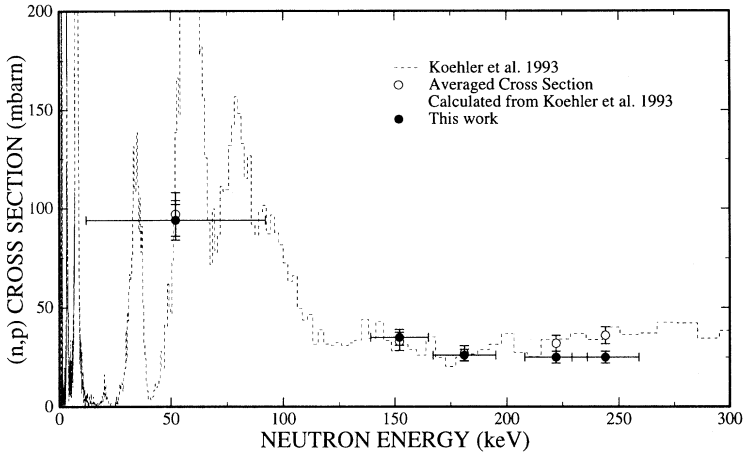

FIG. 6. The average cross section results of the present work (filled circles) and the cross section data of Koehler *et al.* [11] (dashed line). For comparison, the average cross sections for the neutron spectra used in this work were calculated from the Koehler *et al.* data (open circles). The horizontal bars represent the FWHM of the neutron distributions.

Since there are no differential data for the $^{36}Cl(n,\alpha)^{33}P$ reaction, the stellar reaction rate listed in Table V could only be estimated. Assuming that the neutron spectrum at 52 keV resembles approximately a Maxwell-Boltzmann spectrum, and that the reaction rate follows the calculated shape of Woosley *et al.* [24], the stellar cross section for the $^{36}Cl(n,\alpha)^{36}S$ reaction could be extrapolated to kT=30 keV:

$$\frac{\langle \sigma \times v \rangle}{v_T} = 0.91 \pm 0.2 \text{ mb}. \quad (6)$$

Note that the quoted uncertainty does not include the uncertainty of the extrapolation to kT=30 keV. This result is about 20% lower than the theoretical value of Woosley *et al.* [24] of 1.15 mb. Furthermore, it is a factor of 100 smaller than the cross section for the (n,p) channel, and thus of minor astrophysical importance (Sec. V B).

V. PRODUCTION OF ^{36}S BY THE WEAK *s*-PROCESS COMPONENT

A. Nucleosynthesis network

The *s*-process in the sulfur region was investigated using the nucleosynthesis code NETZ [12]. The network contained 30 nuclei between ^{28}Si and ^{42}Ca and a total of 47 reactions including neutron captures and β decays.

Since NETZ is a code for the numeric solution of a set of differential equations, the information from stellar evolution must be included via time dependent profiles for temperature, mass density, and neutron density averaged over the considered burning zones. These parameters were adopted from Raiteri [26] and Raiteri *et al.* [27] for the evolution of a $25M_\odot$ star during the hydrogen, helium, and carbon burning stages. In this model, the *s*-process during convective core helium burning lasts 160 000 yr at a temperature of 30 keV and an electron density on the order of 10^{27} cm^{-3}. During the subsequent stage of convective shell carbon burning *s*-process nucleosynthesis continues for a relatively short period of 0.66 yr but at a higher temperature (kT = 86 keV) and electron density ($n_e = 3\times10^{28}$ cm^{-3}).

TABLE V. Stellar cross sections (mb).

Thermal energy (keV)	Reaction $^{33}S(n,\alpha)^{30}Si$	$^{36}Cl(n,p)^{36}S$	$^{36}Cl(n,\alpha)^{33}P$
20	162	89	1.1
25	175±9	91	1.0
30	181	91±8	0.9±0.2
40	182	86	0.8
60	156	73	0.7
100	100	55	0.7

Stellar models for *s*-process nucleosynthesis in massive stars are still hampered by the relatively large uncertainties of nuclear reaction rates, especially for the key reactions $^{12}C(\alpha,\gamma)^{16}O$, which has strong impact on stellar evolution, and for $^{22}Ne(\alpha,n)^{25}Mg$, which determines the neutron production. Nevertheless, Raiteri *et al.* [10] succeeded in reproducing the solar abundances of the *s*-only isotopes in the $70<A<90$ mass range. From a nucleosynthesis point of view, their choice of *s*-process parameters appears therefore quite consistent.

The nuclear reaction cross sections employed in this calculation are included in Table VI. If experimental cross sections were not available, the theoretical reaction rates of Woosley *et al.* [24] were adopted. The required β-decay rates were taken from Takahashi and Yokoi [28] and at higher temperatures and densities from Neuberger [29]. A solar composition [1] was assumed for the initial seed distribution (Table IX).

B. Results of the network calculations

The results obtained in this study are affected by limitations related to (i) uncertainties in the stellar model, in particular for the shell carbon-burning stage, (ii) a nonsolar distribution of seed abundances, (iii) the possibility that the *s*-process abundances could have been modified by explosive events at the end of stellar evolution, and (iv) the fact that this investigation does not account for galactic chemical evolution but is restricted to a 25 $M_\odot$ star. Therefore, the direct comparison with solar abundances is rather uncertain. These calculations are useful mainly to identify the relevant *s*-process rates for the production of ^{36}S as well as to provide estimates for the relative contributions from the different burning zones.

TABLE VI. Sensitivity of the ^{36}S abundance with respect to cross sections.

Reaction[a]	Sensitivity[b]		$\langle\sigma v\rangle/v_T$	Type[c] and
	He burning	He+C burning	(mb) at 30 keV	reference[d]
$^{34}S(n,\gamma)$	0.66	0.63	2.93	t
$^{35}Cl(n,\gamma)$	0.65	0.49	10.0	e
$^{36}Cl(n,p)$	0.31	0.23	91	e, this work
$^{33}S(n,\alpha)$	-0.25	-0.30	181	e, this work
$^{33}S(n,\gamma)$	0.15	0.17	7.40	e
$^{32}S(n,\gamma)$	0.13	0.15	4.70	e
$^{36}Cl(n,\gamma)$	-0.11	-0.10	11.9	t
$^{36}S(n,\gamma)$	-0.03	-0.04	0.31	t
$^{36}Cl(n,\alpha)$	-0.008	-0.008	0.9	e, this work
$^{38}Ar(n,\gamma)$	0.008	0.07	2.60	t
$^{37}Cl(n,\gamma)$	0.003	0.02	2.15	e
$^{31}P(n,\gamma)$	0.001	0.002	1.74	e
$^{36}Ar(n,\gamma)$	0.001	0.006	8.00	e
$^{33}S(n,p)$	<0.001	<0.001	0.48	t
$^{35}Cl(n,p)$	<0.001	-0.005	1.87	e, [32]
$^{37}Ar(n,\alpha)$	<0.001	0.002	692	t, [24]
$^{39}Ar(n,\gamma)$	<0.001	-0.01	8.11	t

[a]Ordered according to sensitivity during He burning.
[b]Change of ^{36}S abundance / change of cross section.
[c]e: experimental, t: theoretical.
[d]If not specified, values are from [25].

In a first step, the network was tested by comparison with the results of Raiteri *et al.* [10], using the same set of reaction rates. The good agreement obtained in this test justified the simplification of using effective profiles for temperature, electron density, and mass density instead of averaging the produced abundances from different mass zones.

Next, the new experimental $^{36}Cl(n,p)$ and $^{36}Cl(n,\alpha)$ cross sections were implemented in the network illustrated in Fig. 7 for the He burning phase. The situation during C burning is roughly the same with a few exceptions discussed below. Important branching points of the network were identified at the isotopes ^{33}S, ^{35}S, ^{35}Cl, ^{36}Cl, and ^{39}Ar. The corresponding branching ratios were calculated from the time integrated reaction flows and are shown in Table VII. At ^{33}S, the (n,α) channel is clearly dominating, leading to a strong recycling to ^{30}Si, which shields ^{36}S from the abundant seed nuclei ^{28}Si and ^{32}S.

The actual production of ^{36}S is determined by the following three branchings: (1) During He burning the entire flow reaching ^{35}S is directed via β decay to ^{35}Cl. Only at the higher temperatures during C burning, the (n,γ) channel opens up resulting in a 10% branching towards ^{36}S. The main contributions to ^{36}S are, however, due to the branchings at ^{36}Cl and ^{39}Ar. (2) At ^{36}Cl, the (n,p) channel dominates during both burning stages. Therefore, most of the reaction flow from lighter seed nuclei reaching the chlorine isotopes is converted into ^{36}S.

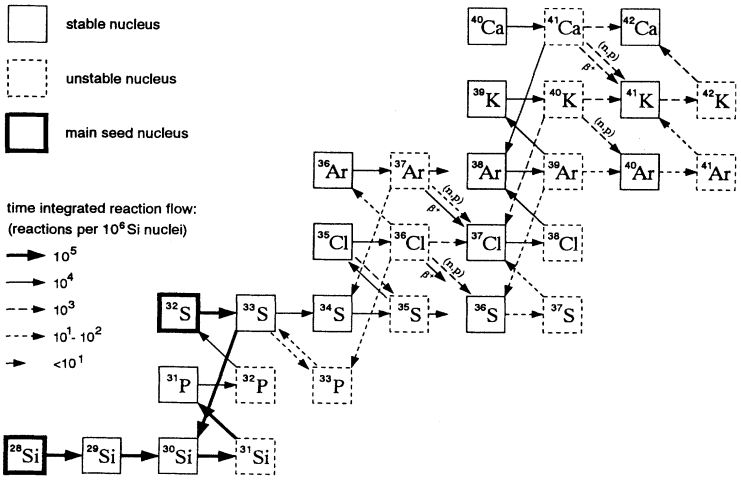

FIG. 7. The time integrated *s*-process flow in the mass region between ^{28}Si and ^{42}Ca during He burning. The process is mostly determined by neutron captures on the abundant seed nuclei, ^{28}Si and ^{32}S. The production of ^{36}S is sensitive to the interplay of the branchings at ^{33}S, ^{36}Cl, and ^{39}Ar.

TABLE VII. Branching points in reaction flow.

Isotope	Channel	Reaction flow (%)	
		He burning	C burning
^{33}S	(n,α)	96	96
	(n,γ)	3.9	3.0
	(n,p)	0.25	0.84
^{35}S	(β^-)	100	90
	(n,γ)	0	10
^{35}Cl	(n,γ)	84	64
	(n,p)	16	37
^{36}Cl	(n,p)	85	90
	(n,γ)	11	8.9
	(β^-)	3	0
	(n,α)	0.84	1.08
^{39}Ar	(β^-)	99	0.85
	(n,γ)	0.83	65
	(n,α)	0.33	35

(3) A third contribution to the ^{36}S abundance comes from the $^{39}Ar(n,\alpha)^{36}S$ reaction. The relative importance of each of these reaction sequences to ^{36}S is shown in Table VIII. During He burning, the ^{36}S production is dominated by the $^{36}Cl(n,p)$ reaction, while the $^{39}Ar(n,\alpha)$ and $^{35}S(n,\gamma)$ reactions are only important during the C-burning stage.

The time dependence of some isotopic abundances during the He and C burning episodes is shown in Fig. 8. While most isotopes in the mass region between Si and Ar exhibit only minor changes during He burning, the abundances of ^{36}S, ^{37}Cl, and ^{40}Ar, which are dominated by the s-process, are clearly increasing. This confirms the observation of Prantzos *et al.* [30] that the final abundances of these isotopes are determined by the total neutron exposure during the s-process. This holds in particular for ^{36}S, where most of the mass flow from lighter elements is accumulated because its small (n,γ) cross section allows only about 3% of the mass flow to proceed. Since the s-abundance of ^{36}S can be reliably determined using the experimentally determined cross sections, this isotope is

TABLE VIII. s-process contributions to ^{36}S production.

Reaction	Contributions in %		
	He burning	C burning	He+C burning
$^{36}Cl(n,p)$	99.1	62.3	87.7
$^{39}Ar(n,\alpha)$	0.8	24.2	8.1
$^{35}S(n,\gamma)$	0.0	13.5	4.2
$^{36}Cl(\beta^-)$	0.1	0.0	0.0
for total production	68.7	31.3	100.0

well suited for testing the neutron exposure predicted by stellar models for He and C burning in massive stars.

During C burning, constant abundances are quickly established due to the steeply decreasing neutron density. During that stage, the ^{36}S abundance is increased by 30% (Table VIII). The strong enhancement of ^{39}Ar is due to the very short time scale of C burning compared to the 260 yr half-life of this isotope.

The overabundances obtained in the calculation (produced abundance/seed abundance) are presented in Fig. 9. As for the significant s-production of ^{36}S, ^{37}Cl, and ^{40}Ar, these results are in good agreement with the work of Raiteri *et al.* [27]. The overproduction factors for ^{36}S (78 after He burning and 108 after subsequent C burning) are about 10% smaller than those reported before (94 and 117, respectively) [26,27]. The weak impact of the new $^{36}Cl(n,p)$ cross section, which is about two times smaller than previously adopted [24], results from the branching at ^{36}Cl. This branching remains to be dominated by the (n,p) channel, which accounts for 85% of the reaction flow during He burning and for 90% during C burning (Table VII). Accordingly, the ^{36}Ar abundance is significantly depleted during the s-process.

The influence of the $^{33}S(n,\alpha)$ rate was examined with respect to the four times larger value of [23]. The present cross section leads to a 30% increase in the ^{36}S abundance due to the reduced recycling to ^{30}Si.

The sensitivity of the ^{36}S abundance to various other cross sections was investigated to identify the important reactions and to explore the possible impact of further cross section measurements. This study was performed

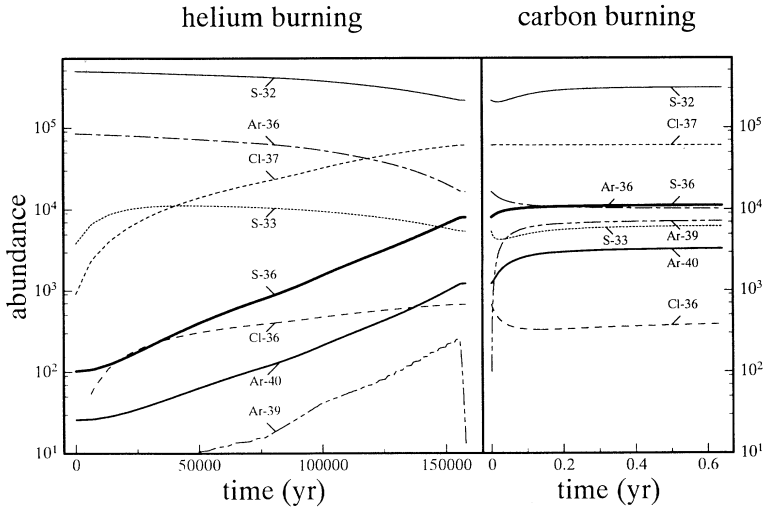

FIG. 8. The abundance changes of selected isotopes during the He and C burning stages.

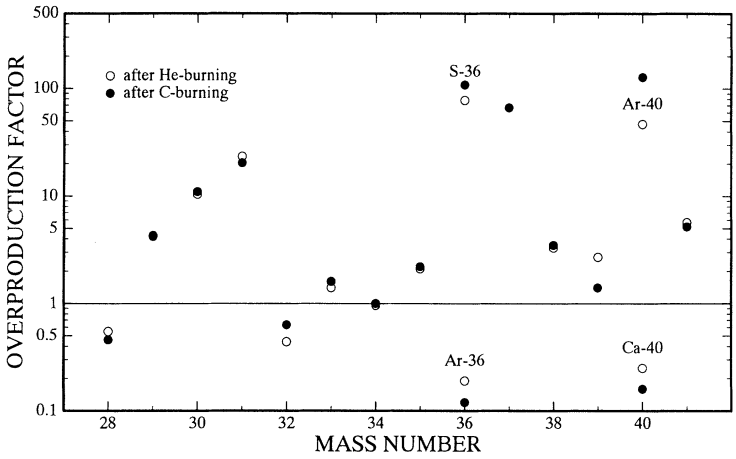

FIG. 9. The resulting overabundances as a function of atomic mass. Open circles indicate the abundances after He burning, while the final abundances after He and C burning are given by filled circles.

by repeating the complete network for each of these isotopes, after the respective cross sections were changed by a factor 2. The sensitivity of the ^{36}S production was then defined as the ratio of the relative change of the ^{36}S abundance to the relative variation of the various cross sections (+100% or −50%, respectively).

The results presented in Table VI do not depend on whether the rates are increased or decreased. It is found that the here-presented cross sections for $^{36}\mathrm{Cl}(n,p)^{36}\mathrm{S}$ as well as for $^{33}\mathrm{S}(n,\alpha)^{30}\mathrm{Si}$ are among the most sensitive parameters, thus providing a significant improvement of the nuclear physics input for the synthesis of ^{36}S. Interestingly, $^{34}\mathrm{S}(n,\gamma)^{35}\mathrm{S}$ was identified as the most important reaction. This was already found by Howard *et al.* [3], but for a completely different stellar scenario. Because of its low (n,γ) cross section, ^{34}S acts as a bottle neck for the reaction flow to ^{36}S. While the next three important reactions have all been investigated experimentally [$^{35}\mathrm{Cl}(n,\gamma)$ by Macklin [31]], only theoretical calculations exist for the $^{34}\mathrm{S}(n,\gamma)$ rate. Since the remaining uncertainty for the *s*-process abundance of ^{36}S is determined by this rate, a measurement of the $^{34}\mathrm{S}(n,\gamma)^{35}\mathrm{S}$ cross section would be highly desirable. All other reactions are of minor influence unless their cross sections were subject to drastic changes.

Similar overproduction factors as for ^{36}S are obtained for ^{37}Cl via (n,γ) reactions on ^{36}Ar and subsequent EC decays as well as for ^{40}Ar, which is mainly produced by $^{40}\mathrm{K}(n,p)$ reactions. The corresponding *s* process yields are comparably uncertain, since experimental reaction rates are still missing in both cases. This deficiency hampers the quantitative discussion of the chronometric pair $^{40}\mathrm{K}/^{40}\mathrm{Ar}$ [8].

Finally, the influence of the seed abundances on the ^{36}S production was examined. Again, the sensitivity was defined as the ratio of the change in ^{36}S production to the variation of the seed abundance. The abundances of the relevant seed nuclei were changed by a factor 2, but seed nuclei with sensitivities smaller than 0.005 were neglected. The results are presented in Table IX. It was found that the synthesis path for ^{36}S can be restricted to the mass region $A > 32$, since ^{32}S, ^{34}S, and ^{35}Cl are the only relevant seed nuclei. This means that even during the long period of He burning almost no nuclei lighter than sulfur are processed to ^{36}S. The increasing sensitivity to heavier seed nuclei during C burning reflects the increasing importance of the $^{39}\mathrm{Ar}(n,\alpha)$ reaction (Table VIII).

TABLE IX. Sensitivity of the ^{36}S abundance with respect to seed abundances.

Isotope	Sensitivity[a]		Seed abundance[b]
	He burning	He+C burning	
^{34}S	0.58	0.55	2.17×10^{4}
^{35}Cl	0.24	0.18	2.86×10^{3}
^{32}S	0.15	0.18	4.89×10^{5}
^{40}Ca	0.004	0.05	5.92×10^{4}
^{38}Ar	0.002	0.02	1.60×10^{4}

[a]Change of ^{36}S abundance / change of seed abundance.
[b]Relative to 10^{6} Si atoms, [1].

VI. CONCLUSIONS

The measurement of the $^{33}\mathrm{S}(n,\alpha)$, the $^{36}\mathrm{Cl}(n,p)$, and the $^{36}\mathrm{Cl}(n,\alpha)$ cross sections in the keV energy range removed ambiguities of former experiments and led to an improvement of the nuclear reaction data of relevance for the origin of the rare neutron rich isotope ^{36}S. This information was used for an analysis of the ^{36}S production during the *s*-process in $25\mathrm{M}_{\odot}$ star.

As a result of the new $^{36}\mathrm{Cl}(n,p)$ rate the calculated production factors of ^{36}S during the He and C burning phases were found to about 10% lower than reported by Raiteri *et al.* [10]. Nevertheless, this study confirms that a significant fraction (if not all) of this isotope can be produced in massive stars. Various sensitivity tests showed (i) that only ^{32}S, ^{34}S, and ^{35}Cl need to be considered as the seed nuclei for an *s*-process production of ^{36}S, and (ii) that the $^{34}\mathrm{S}(n,\gamma)^{35}\mathrm{S}$ cross section is the only missing

experimental information in the nuclear physics data set related to the s-process production of ^{36}S. All other cross sections have been determined by experiments or are not relevant for the resulting ^{36}S abundance.

Since the ^{36}S production was confirmed to be a sensitive tool for determining the total neutron exposure during the s-process in massive stars, an experimental determination of the $^{34}S(n,\gamma)$ cross section appears well justified and would allow a quantitative discussion of this aspect.

ACKNOWLEDGMENTS

We gratefully acknowledge the technical assistance of G. Rupp during the detector construction and the experiments. We would also like to thank A. Ernst, H.-P. Knaetsch, D. Roller, and W. Seith of the accelerator group for the continuous support, C. M. Raiteri for the many helpful discussions on the s-process, and B. Strehlau for the implantation of the sulfur samples.

[1] E. Anders and N. Grevesse, Geochim. Cosmochim. Acta **53**, 197 (1989).
[2] D. Arnett and F. K. Thielemann, Astrophys. J. **295**, 589 (1985).
[3] W. M. Howard, W. D. Arnett, D. D. Clayton, and S. Woosley, Astrophys. J. **175**, 201 (1972).
[4] T. A. Weaver and S. E. Woosley, Phys. Rep. **227**, 65 (1993).
[5] F. Käppeler, H. Beer, and K. Wisshak, Rep. Prog. Phys. **52**, 945 (1989).
[6] R. G. Couch, A. B. Schmiedekamp, and D. Arnett, Astrophys. J. **190**, 95 (1974).
[7] S. Lamb, W. M. Howard, and J. W. Truran, Astrophys. J. **217**, 213 (1977).
[8] H. Beer and R. D. Penzhorn, Astron. Astrophys. **174**, 323 (1987).
[9] N. Langer, J.-P. Arcoragi, and M. Arnould, Astron. Astrophys. **210**, 187 (1989).
[10] C. M. Raiteri, M. Busso, R. Gallino, G. Picchio, and L. Pulone, Astrophys. J. **367**, 228 (1991).
[11] P. E. Koehler, S. M. Graff, H. A. O'Brian, Yu. M. Gledenov, and Yu. P. Popov, Phys. Rev. C **47**, 2107 (1993).
[12] S. Jaag, Technical report, Kernforschungszentrum Karlsruhe (unpublished).
[13] H. Beer and F. Käppeler, Phys. Rev. C **21**, 534 (1980).
[14] W. Ratynski and F. Käppeler, Phys. Rev. C **37**, 595 (1988).
[15] H. Schatz, F. Käppeler, M. Wiescher, and P. E. Koehler, Astrophys. J. **413**, 750 (1993).
[16] H. Liskien and A. Paulsen, At. Data Nucl. Data Tables **15**, 57 (1975).
[17] M. Wiescher, R. Steiniger, and F. Käppeler, Astrophys. J. **344**, 464 (1989).
[18] R. L. Macklin, private communication.
[19] R. Steininger, Diplom thesis, University of Karlsruhe, 1988.
[20] H. Schatz, Diplom thesis, University of Karlsruhe, 1992.
[21] B. B. Rossi and H. H. Staub, *Ionization Chambers and Counters* (McGraw-Hill, New York, 1949).
[22] C. Wagemans, H. Weigmann, and R. Barthelemy, Nucl. Phys. **A469**, 497 (1987).
[23] G. F. Auchampaugh, R. L. Halperin, R. L. Macklin, and W. M. Howard, Phys. Rev. C **12**, 1126 (1975).
[24] S. E. Woosley, W. A. Fowler, J. A. Holmes, and B. A. Zimmerman, At. Data Nucl. Data Tables **22**, 371 (1978).
[25] Z. Y. Bao and F. Käppeler, At. Data Nucl. Data Tables **36**, 411 (1987).
[26] C. M. Raiteri, private communication.
[27] C. M. Raiteri, M. Busso, R. Gallino, and G. Picchio, Astrophys. J. **371**, 665 (1991).
[28] K. Takahashi and K. Yokoi, At. Data Nucl. Data Tables **36**, 375 (1987).
[29] D. Neuberger, Diplom thesis, University of Karlsruhe, 1991.
[30] N. Prantzos, M. Arnould, and J.-P. Arcoragi, Astrophys. J. **315**, 209 (1987).
[31] R. L. Macklin, Phys. Rev. C **29**, 1996 (1984).
[32] S. Druyts, C. Wagemans, and P. Geltenbort, Nucl. Phys. **573**, 291 (1994).